

Manuscript version: Author's Accepted Manuscript

The version presented in WRAP is the author's accepted manuscript and may differ from the published version or Version of Record.

Persistent WRAP URL:

<http://wrap.warwick.ac.uk/146554>

How to cite:

Please refer to published version for the most recent bibliographic citation information. If a published version is known of, the repository item page linked to above, will contain details on accessing it.

Copyright and reuse:

The Warwick Research Archive Portal (WRAP) makes this work by researchers of the University of Warwick available open access under the following conditions.

© 2020 Elsevier. Licensed under the Creative Commons Attribution-NonCommercial-NoDerivatives 4.0 International <http://creativecommons.org/licenses/by-nc-nd/4.0/>.



Publisher's statement:

Please refer to the repository item page, publisher's statement section, for further information.

For more information, please contact the WRAP Team at: wrap@warwick.ac.uk.

Vibration and power regulation control of a floating wind turbine with hydrostatic transmission

Xin Tong, Xiaowei Zhao*

School of Engineering, University of Warwick, Coventry CV4 7AL, United Kingdom

Abstract

We design a blade pitch controller employing linear parameter-varying (LPV) synthesis techniques for a floating hydrostatic wind turbine (HWT) with a barge platform, which is based on the LIDAR (Light Detection and Ranging) preview on the wind speed. The developed control system can simultaneously reduce barge pitch motions and regulate the power in Region 3. These two functions would normally disturb each other if designed separately. The state space model is not affinely dependent on the wind speed thus the LPV controller is obtained by satisfying multiple LMIs evaluated at a set of gridded points within the wind speed range in Region 3. An anti-windup compensation scheme is then used to improve the LPV controller's performance when the pitch undergoes saturation around the rated wind speed. The simulations based on a high-fidelity barge HWT model show that our pitch controller significantly reduces barge pitch motions, loads on blade bearings & tower, and generator power fluctuations, compared with a gain-scheduled PI pitch controller.

Keywords: Hydrostatic wind turbine, floating barge, vibration reduction, power regulation, linear parameter varying control, LIDAR preview

1. Introduction

There has been a significant surge in global energy demand due to population explosion and massive-scale industrialisation. A number of countries have seen that energy is consumed much faster than being produced [1].

*Corresponding author.

E-mail address: xiaowei.zhao@warwick.ac.uk (X. Zhao)

5 High energy demand has driven extensive usage of fossil fuels which are the
6 main cause of air pollution and global warming [2]. To tackle these issues,
7 many countries have embraced renewable energy sources to replace fossil fu-
8 els. Wind is one of the most widely used renewable energy sources [3].

9 Worldwide wind installations have been significantly increasing. By the
10 end of 2019, the global installed wind power capacity had reached over 651
11 GW [4], surging from only 74 GW in 2006 [5]. The United Kingdom aims
12 to install 40 GW of offshore wind power by 2030 [6]. By the same year, the
13 EU is estimated to install 323 GW of wind power capacity which will meet
14 30% of the EU power demand. This will save Europe €382 million total
15 CO₂ emissions in 2030 [7]. Wind power is predicted to make up more than
16 one-third of world electricity generation by 2050 [8].

17 The gearbox of a conventional offshore wind turbine is one of the largest
18 contributors to its overall operation & maintenance (O&M) costs [9, 10]. The
19 gearbox suffers a high failure rate which grows further as the offshore turbine
20 is being built increasingly large. The paper [10] showed that replacement of a
21 gearbox required an average of 17.2 technicians with an average replacement
22 cost of €230,000. Besides, the gearbox causes the longest downtime per
23 failure among all the turbine components [11]. Based on the calculation by
24 Ran et al. [12], the daily average revenue loss during the downtime of a
25 4-MW offshore turbine can be £6,720.

26 To address the above gearbox reliability issue, hydrostatic wind turbines
27 (HWTs) were proposed. It uses a more reliable hydrostatic transmission
28 (HST) drivetrain to replace the gearbox one. Figure 1 represents a typical
29 HST drivetrain [13, 14]. A hydraulic pump is connected to the turbine rotor
30 shaft, which transfers wind power into a high-pressure oil flow. A hydraulic
31 motor then converts the oil flow into mechanical power to drive an electric
32 generator. The required transmission ratio is achieved by the displacement
33 ratio between the pump and the motor. Thus a variable-displacement mo-
34 tor allows continuously varying transmission ratios so that a synchronous
35 generator can be used.

36 An HWT has 3 major regions of operation manipulated by torque and
37 pitch controls, which is the same as a conventional wind turbine. In the
38 present paper we consider Region 3 when the wind speed is above the rated
39 speed, where both controllers work together to maintain the rotor speed
40 & generator power around rated values. In this region, the platform of a
41 floating wind turbine often has large pitch motions due to high winds/waves.
42 It brings about large load fluctuations (especially on the tower base) and

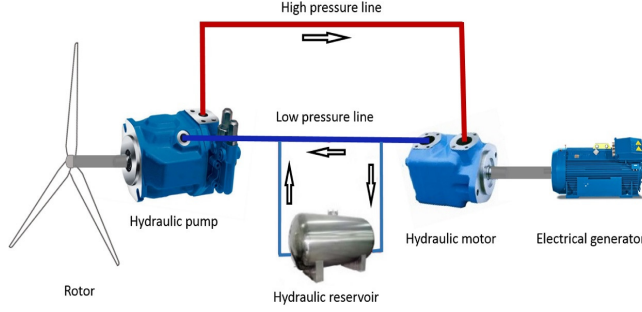


Figure 1: The main components and their connections of a typical HST drivetrain in the HWT. This figure is taken from the literature [14]

significant variations in the rotor speed & generator power [15], which causes damage and reduces fatigue life. Thus, control techniques are required to suppress these platform motions.

The literature [13, 16, 17] designed pitch controllers using a simple model which only considered the angular rotation of the rotor/pump shaft. The papers [13, 17] adopted PI control on the error between the filtered rotor speed and its rated value. The PI controller in [13] had constant gains and was derived based on a single-DOF (degree of freedom) model linearised at an operating point. Laguna [17] employed a PI controller with the proportional and integral gains adjusted by the blade pitch angle. Skaare et al. [16] proposed gain-scheduled integral control on the error between the aerodynamic power and its command with the pitch angle as the scheduling parameter, based on an aerodynamic power estimator. Dolan and Aschemann [18] developed a gain-scheduled linear quadratic regulator (LQR) which controlled the motor displacement and blade pitch angle simultaneously, with the wind speed as the scheduling parameter. Kersten and Aschemann [19] designed an LQR to control the rotor speed through adjusting the motor displacement. Blade pitch control was employed to damp HWT tower vibrations, based on the feedback of tower-top translational velocities. Two types of blade pitch controllers were designed: an LQR with the feedback gain scheduled by the wind speed and a Lyapunov-based controller with a constant feedback gain. Simplified HWT models were used to test the above controllers, which neglected blade flexibility, ignored tower dynamics or considered only the first tower bending mode, and were not floating. In addition, none of the

above controllers was designed by combining power generation control with structural vibration reduction.

In our paper [20], we designed a loop-shaping torque controller and a linear parameter varying (LPV) collective blade pitch controller for power generation control of a monopile HWT. The LPV pitch controller was scheduled by the LIDAR (Light Detection and Ranging)-previewed steady rotor effective wind speed (REWS). However, abnormal transients could occur during the transition region (between Region 2 and 3) because of saturated blade pitch angles. To avoid them, an anti-windup (AW) compensator was added to the LPV controller. The simulations based on a detailed monopile HWT model validated satisfactory tracking capability of the torque controller and significantly enhanced performances of the LPV pitch controller compared with a gain-varied PI pitch controller.

In the present paper we are interested in extending our research results in [20] to floating HWTs for which vibration control of the floating platform is critical (as mentioned earlier). We consider a barge platform. Compared with [20], turbine fore-aft (pitch) dynamics are taken into account for the design of the torque and blade pitch controllers. Most importantly, the LPV controller designed in the paper [20] had a single input and a single output, and was used to regulate power only, while the LPV controller in the present paper has multiple inputs and can regulate power and damp barge pitch motions simultaneously. Besides, in [20] the state space model for the LPV control design is affinely dependent on the wind speed, so the LPV controller was obtained by only satisfying two LMIs at the vertices of the Region-3 wind speed range while the state space model in the present paper is not affinely dependent on the wind speed thus the LPV controller is obtained by satisfying multiple LMIs evaluated at a set of gridded points within the Region-3 wind speed range. We mention that if power regulation control and barge vibration control are designed separately (both using blade pitch actuation), they normally disturb each other. Hence here we aim at developing a blade pitch control technique for floating HWTs to tackle power regulation and large platform vibrations during Region-3 operation in a synthetic manner. More specifically, we focus on turbine pitch (fore-aft) vibrations because the fore-aft direction suffers the largest loading from winds and waves [15].

We assess the designed control system using a high-fidelity barge HWT simulation model taking into account aerodynamics, hydrodynamics, servodynamics, and elastic dynamics. This model is constructed through replacing the gearbox drivetrain of the widely-used NREL (National Renewable Energy

105 Laboratory) 5-MW barge wind turbine model (built based on the FAST
 106 (Fatigue, Aerodynamics, Structures, and Turbulence) code) with an HST
 107 drivetrain. A similar transformation procedure was expatiated upon in our
 108 paper [20] for a turbine with a monopile substructure, and therefore is not
 109 iterated here. The simulation results demonstrate that the proposed pitch
 110 controller regulates multiple responses (including the rotor speed, generator
 111 power, loads on the tower and blade pitch bearings, and barge pitch motions)
 112 considerably better than a gain-varied PI pitch controller.

113 The paper is organised as below. A control-oriented model and an LPV
 114 blade pitch controller with AW ability are developed in Section 2. Simulation
 115 studies are carried out in Section 3 for the proposed control system, using
 116 the NREL 5-MW HWT model (transformed) with a floating barge platform.
 117 Discussion is given in Section 4 while Section 5 concludes this paper.

118 2. Pitch Control Design of A Barge HWT

119 This paper uses the HST mathematical model from Laguna [17], and the
 120 parameters therein. The design of the (\mathcal{H}_∞ loop-shaping) torque controller
 121 for the floating HWT is similar as in our paper [20] except that here the
 122 control design model includes pitch dynamics of the barge platform. Thus
 123 we omit it and refer [20] for details. In this paper we focus on the design of
 124 pitch control which is very different from [20].

125 2.1. Modelling

126 The design of the HWT pitch controller is based on the dynamics of the
 127 rotor/pump shaft, turbine's fore-aft (pitch) motions and blade pitch actuator.
 128 Dynamics of the flexible blades and turbine's side-to-side motions are not
 129 considered because the blade pitch controller is designed to tackle fore-aft
 130 vibrations of the floating HWT. Study on the reduction of blade and turbine's
 131 side-to-side loads is not covered in this research.

The rotor/pump shaft dynamics are

$$\dot{\omega}_r = \frac{1}{J_r + J_p}(\tau_a - \tau_p), \quad (2.1)$$

132 where ω_r is the shaft speed of the coupled rotor & pump. τ_a is the aero-
 133 dynamic torque. The parameters J_p and J_r are the rotational inertia of the
 134 pump and rotor, respectively. The pump torque τ_p is

$$\tau_p = D_p P_p + B_p \omega_r + C_{fp} D_p P_p \quad (2.2)$$

where the displacement, viscous damping coefficient, and Coulomb friction coefficient are represented by D_p , B_p , and C_{fp} , respectively. P_p is the pressure difference across the pump.

The turbine's pitch motion, Σ_p , is assumed to be like the pitch motion of an inverted pendulum fixed on a rigid platform. Then its kinetic energy T_{op} and potential energy V_{op} are

$$\begin{aligned} T_{op} &= \frac{1}{2}I_{tp}\dot{\theta}_T^2 + \frac{1}{2}I_{bp}\dot{\theta}_P^2, \\ V_{op} &= \frac{1}{2}k_{tp}(\theta_T - \theta_P)^2 + \frac{1}{2}(C_{hs} + C_{ml})\theta_P^2 + m_tgL_t \cos \theta_T - m_pgL_p \cos \theta_P, \end{aligned} \quad (2.3)$$

where θ_T and θ_P are the tower's rotational pitch displacement and barge's pitch displacement, respectively. C_{hs} is the hydrostatic restoring coefficient for the pitch DOF while C_{ml} is the linearised total mooring line restoring coefficient for the pitch DOF. The pitch inertia of the tower-rotor-nacelle assembly and barge are represented by I_{tp} and I_{bp} , respectively. They are defined with respect to the pitch axis (denoted by y_i) of the inertial turbine coordinate system set by FAST [21]. m_p and m_t are the barge mass and total mass of the tower-rotor-nacelle assembly, respectively. k_{tp} is the restoring coefficient of the tower-rotor-nacelle assembly for the pitch DOF. L_t and L_p are the distance from the centre of mass of the tower-rotor-nacelle assembly to y_i , and the distance from the centre of mass of the barge to y_i , respectively. g is the acceleration of gravity on Earth.

Then Σ_p is derived by the Lagrange's equation approach

$$\begin{aligned} \frac{d}{dt} \left(\frac{\partial \mathcal{L}_{op}}{\partial \dot{\theta}_T} \right) - \frac{\partial \mathcal{L}_{op}}{\partial \theta_T} &= f_T, \\ \frac{d}{dt} \left(\frac{\partial \mathcal{L}_{op}}{\partial \dot{\theta}_P} \right) - \frac{\partial \mathcal{L}_{op}}{\partial \theta_P} &= f_P, \\ \mathcal{L}_{op} &= T_{op} - V_{op}, \end{aligned} \quad (2.4)$$

where

$$\begin{aligned} f_P &= -A_{rad}\ddot{\theta}_P - (B_{rad} + B_{vis})\dot{\theta}_P + d_{tp}(\dot{\theta}_T - \dot{\theta}_P) + M_w, \\ f_T &= -d_{tp}(\dot{\theta}_T - \dot{\theta}_P) + F_aL_{hh}. \end{aligned} \quad (2.5)$$

Here A_{rad} and B_{rad} are the radiation-induced hydrodynamic added moment of inertia and damping coefficient for the pitch DOF, respectively. B_{vis} is

the viscous-drag-induced linearised hydrodynamic damping coefficient for the pitch DOF. d_{tp} is the damping coefficient of the tower-rotor-nacelle assembly for the pitch DOF. M_w is the total excitation moment exerted by waves about y_i . F_a is the aerodynamic rotor thrust acting on the hub and the distance from it to y_i is approximately the hub height above the mean sea level denoted by L_{hh} . The ways to derive the values of m_t , m_p , L_{hh} , I_{tp} , I_{bp} , L_t , L_p , k_{tp} , d_{tp} , C_{hs} , A_{rad} , B_{rad} , B_{vis} , and C_{ml} in (2.3) and (2.5) can be found in our previous paper [22].

The nonlinear terms τ_a in (2.1) and F_a in (2.5) depend on ω_r (shaft speed of the coupled rotor & pump), V (REWS), $\dot{\theta}_T$ (tower pitch velocity), and β (blade pitch angle). The small deviations of them from an operating point op can be linearised as

$$\begin{aligned}\hat{\tau}_a &= \frac{\partial \tau_a}{\partial \omega_r} \Big|_{op} \hat{\omega}_r + \frac{\partial \tau_a}{\partial V} \Big|_{op} (\hat{V} - L_{hh} \dot{\hat{\theta}}_T) + \frac{\partial \tau_a}{\partial \beta} \Big|_{op} \hat{\beta}, \\ \hat{F}_a &= \frac{\partial F_a}{\partial \omega_r} \Big|_{op} \hat{\omega}_r + \frac{\partial F_a}{\partial V} \Big|_{op} (\hat{V} - L_{hh} \dot{\hat{\theta}}_T) + \frac{\partial F_a}{\partial \beta} \Big|_{op} \hat{\beta},\end{aligned}\tag{2.6}$$

where $\hat{x} = x - \bar{x}$ (the bar over the variable denotes its steady value at op). The coefficients $\frac{\partial \tau_a}{\partial \omega_r} \Big|_{op}$, $\frac{\partial \tau_a}{\partial V} \Big|_{op}$, $\frac{\partial \tau_a}{\partial \beta} \Big|_{op}$, $\frac{\partial F_a}{\partial \omega_r} \Big|_{op}$, $\frac{\partial F_a}{\partial V} \Big|_{op}$, and $\frac{\partial F_a}{\partial \beta} \Big|_{op}$ are derived through FAST linearisation at op [21].

The blade pitch actuator dynamics are described by

$$\dot{\beta} = \frac{1}{T_\beta} (\beta_r - \beta)\tag{2.7}$$

where β is the actual blade pitch angle while β_r is its reference signal from the blade pitch controller. The time constant T_β of this 1st-order system is 0.1 s.

2.2. LPV Pitch Controller with AW compensation

For Region-3 constant power generation, the relationship $p_r = \tau_p \omega_r$ (where the rated rotor power p_r is 5.2966e6 W) is required. So (2.1) becomes

$$\dot{\omega}_r = \frac{1}{J_r + J_p} \left(\tau_a - \frac{p_r}{\omega_r} \right).\tag{2.8}$$

By combining (2.3)–(2.8), we derive a nonlinear model, which leads to a state-space model \mathbf{G}_p (through linearisation at an operating point op):

$$\dot{\mathbf{x}}_p = \mathbf{A}_p \mathbf{x}_p + \mathbf{B}_p \hat{\beta}_r + \mathbf{B}_{pd} \mathbf{u}_d, \mathbf{y}_p = \mathbf{C}_p \mathbf{x}_p.\tag{2.9}$$

181 $\mathbf{x}_p = [\hat{\omega}_r \quad \hat{\beta} \quad \hat{\theta}_T \quad \dot{\hat{\theta}}_T \quad \hat{\theta}_P \quad \dot{\hat{\theta}}_P]^T$ is the state. $\hat{\beta}_r$ is the input while $\mathbf{y}_p =$
 182 $[\hat{\omega}_r \quad \dot{\hat{\theta}}_P]^T$ is the output which are the deviations of the rotor speed and barge
 183 pitch velocity from their respective steady values. \mathbf{A}_p has the parameter-
 184 varying terms $\hat{\tau}_a$ and \hat{F}_a (see (2.6)) whose coefficients scheduled by $\bar{V} \in \Theta =:$
 $[11.4, 25]\text{m/s}$ in Region3 are shown in Figure 2. Within the entire range of

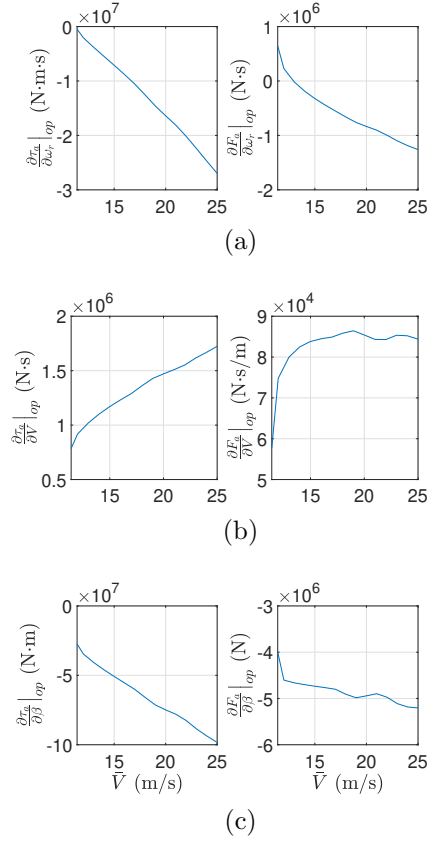


Figure 2: Coefficients in $\hat{\tau}_a$ and \hat{F}_a (see (2.6)) at $\bar{V} \in \Theta =: [11.4, 25]\text{m/s}$.

185 \bar{V} , one value of \bar{V} corresponds to one value of $\bar{\omega}_r$ and one value of $\bar{\beta}$. So (2.9)
 186 can be regarded as an LPV system scheduled only by \bar{V} .

187 The objective of the LPV control design is to find a controller $\mathbf{K}_p(\bar{V})$ that
 188 holds the inequality
 189

$$\|\mathcal{F}\|_{\mathcal{L}_2} = \sup_{\substack{\mathbf{w} \neq \mathbf{0} \\ \bar{V} \in [11.4, 25] \text{ m/s}}} \frac{\|\mathbf{z}\|_2}{\|\mathbf{w}\|_2} < \gamma \quad (2.10)$$

190 where $\|\mathbf{x}\|_2 = \sqrt{\int \mathbf{x}^T \mathbf{x} dt}$. \mathbf{w} is the external signal, which contains the refer-
 191 ence values for $\hat{\omega}_r$ and $\dot{\hat{\theta}}_P$. $\mathbf{z} = [\mathbf{z}_1 \ z_2]^T$ is the performance output, $\|\mathcal{F}\|_{\mathcal{L}_2}$ is
 192 the \mathcal{L}_2 norm from \mathbf{w} to \mathbf{z} , and $\gamma > 0$ represents a performance level. The in-
 193 terconnection for the synthesis of $\mathbf{K}_p(\bar{V})$ is shown in Figure 3. The weighting
 194 functions \mathbf{W}_e and W_u are given by (2.11).

$$\mathbf{W}_e = \begin{bmatrix} W_{e1} & 0 \\ 0 & W_{e2} \end{bmatrix} = \begin{bmatrix} \frac{0.5s+0.3}{s+0.003} & 0 \\ 0 & \frac{5s+9}{s+0.009} \end{bmatrix}, \quad (2.11)$$

$$W_u = \frac{s + 0.19}{0.5s + 0.3}.$$

195 W_{e1} and W_{e2} are selected to have low high-frequency gains to reduce over-
 196 shoots in the time response and have high low-frequency gains (to penalise
 197 the error \mathbf{e}). W_u is selected to limit high-frequency blade pitch control activ-
 ities. In Figure 3, the controller output is $\hat{\beta}_r = \beta_r - \bar{\beta}$ where $\bar{\beta}(\bar{V})$ is shown

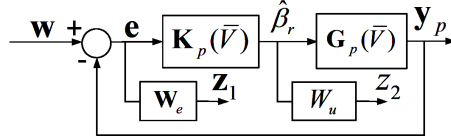


Figure 3: Interconnection for the synthesis of the LPV blade pitch controller $\mathbf{K}_p(\bar{V})$.

198 in Figure 4 and β_r is the actual pitch angle command. As shown in Figure 4,
 199 the pitch rate is high near the rated wind speed of 11.4 m/s. To avoid large
 200 tower loads during the transition between Region 2 and 3 caused by this, $\bar{\beta}$
 201 can be derived as the integral of $\dot{\bar{\beta}}(\bar{V}) = \bar{V} \frac{d\bar{\beta}}{d\bar{V}}(\bar{V})$ where the upper limit of
 202 $d\bar{\beta}/d\bar{V}$ is set to be $2.5^\circ/\text{m}$ [23].

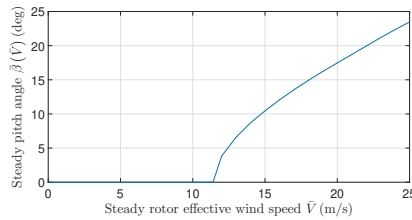


Figure 4: Relationship between the steady pitch angle $\bar{\beta}$ and the steady REWS \bar{V} .

$$\begin{bmatrix} \mathbf{X}\mathbf{A}(\bar{V}) + \tilde{\mathbf{B}}_K\mathbf{C}_2(\bar{V}) + (\star) & \star & \star & \star \\ \tilde{\mathbf{A}}_K^T + \mathbf{A}(\bar{V}) & \mathbf{A}(\bar{V})\mathbf{Y} + \mathbf{B}_2(\bar{V})\tilde{\mathbf{C}}_K + (\star) & \star & \star \\ \left[\mathbf{X}\mathbf{B}_1(\bar{V}) + \tilde{\mathbf{B}}_K\mathbf{D}_{21}(\bar{V})\right]^T & \mathbf{B}_1(\bar{V})^T & -\gamma\mathbf{I} & \star \\ \mathbf{C}_1(\bar{V}) & \mathbf{C}_1(\bar{V})\mathbf{Y} + \mathbf{D}_{12}(\bar{V})\tilde{\mathbf{C}}_K & \mathbf{D}_{11}(\bar{V}) & -\gamma\mathbf{I} \end{bmatrix} < 0 \quad (2.16)$$

203

The interconnection illustrated in Figure 3 is used to synthesise the LPV controller $\mathbf{K}_p(\bar{V})$. Figure 3 gives an open-loop LPV system

$$\dot{\mathbf{x}} = \mathbf{A}(\bar{V})\mathbf{x} + \mathbf{B}_1(\bar{V})\mathbf{w} + \mathbf{B}_2(\bar{V})\hat{\beta}_r, \quad (2.12)$$

$$\mathbf{z} = \mathbf{C}_1(\bar{V})\mathbf{x} + \mathbf{D}_{11}(\bar{V})\mathbf{w} + \mathbf{D}_{12}(\bar{V})\hat{\beta}_r, \quad (2.13)$$

$$\mathbf{y}_p = \mathbf{C}_2(\bar{V})\mathbf{x} + \mathbf{D}_{21}(\bar{V})\mathbf{w}. \quad (2.14)$$

204 Now we determine the stabilising LPV controller $\mathbf{K}_p(\bar{V})$ to satisfy (2.10).
 205 According to [24], first we solve an optimisation problem offline: minimising
 206 $\gamma \left(\mathbf{X}, \mathbf{Y}, \tilde{\mathbf{A}}_K(\bar{V}), \tilde{\mathbf{B}}_K(\bar{V}), \tilde{\mathbf{C}}_K(\bar{V}) \right)$ subject to the LMI (linear matrix in-
 207 equality) constraints (2.15) and (2.16) with \star induced by symmetry.

$$\begin{bmatrix} \mathbf{X} & \mathbf{I} \\ \mathbf{I} & \mathbf{Y} \end{bmatrix} > 0, \mathbf{X} = \mathbf{X}^T > 0, \mathbf{Y} = \mathbf{Y}^T > 0. \quad (2.15)$$

Due to an infinite number of $\bar{V} \in [11.4, 25]$ m/s, an infinite number of LMIs need to be solved, which is infeasible for practical computation. So instead we solve a limited number of LMIs by first gridding the scheduling range of \bar{V} and then deriving LMIs corresponding to the grid points respectively. This sacrifices a certain degree of the nonlinear behaviour of the control-oriented turbine model \mathbf{G}_p (2.9) by assuming that \mathbf{G}_p is affinely dependent on \bar{V} between two adjacent grid points. The density of the grid points should be carefully determined to achieve an acceptable trade-off between satisfaction of this piecewise affine assumption and computational complexity. For \mathbf{G}_p with the dependency on \bar{V} shown in Figure 2, we select the grid points such that $\bar{V} \in \Theta_g =: \{\bar{V} = V_j, j = 1, 2, \dots, 15\}$ where $V_1 = 11.4$ m/s and $V_j = j + 10$ m/s ($j > 1$). Then we derive the controller $K_p(V_j)$ with the

state-space realisation $(\mathbf{A}_K(V_j), \mathbf{B}_K(V_j), \mathbf{C}_K(V_j), 0)$:

$$\mathbf{A}_K(V_j) = \mathbf{N}_p^{-1} \times \left(\tilde{\mathbf{A}}_K(V_j) - \mathbf{X} \mathbf{A}(V_j) \mathbf{Y} - \tilde{\mathbf{B}}_K(V_j) \mathbf{C}_2(V_j) \mathbf{Y} - \mathbf{X} \mathbf{B}_2(V_j) \tilde{\mathbf{C}}_K(V_j) \right) \mathbf{M}_p^{-T}, \quad (2.17)$$

$$\mathbf{B}_K(V_j) = \mathbf{N}_p^{-1} \tilde{\mathbf{B}}_K(V_j), \mathbf{C}_K(V_j) = \tilde{\mathbf{C}}_K(V_j) \mathbf{M}_p^{-T} \quad (2.18)$$

where \mathbf{N}_p and \mathbf{M}_p are the solutions of the factorisation problem $\mathbf{I} - \mathbf{X}\mathbf{Y} = \mathbf{N}_p \mathbf{M}_p^T$. Assuming that \mathbf{A}_p is affinely dependent on \bar{V} between two adjacent grid points, the LPV pitch controller $\mathbf{K}_p(\bar{V})$ thus has the state-space realisation $(\mathbf{A}_K, \mathbf{B}_K, \mathbf{C}_K, 0)$ where

$$\begin{bmatrix} \mathbf{A}_K & \mathbf{B}_K \\ \mathbf{C}_K & 0 \end{bmatrix}(\bar{V}) = \alpha_1 \begin{bmatrix} \mathbf{A}_K(V_j) & \mathbf{B}_K(V_j) \\ \mathbf{C}_K(V_j) & 0 \end{bmatrix} + \alpha_2 \begin{bmatrix} \mathbf{A}_K(V_{j+1}) & \mathbf{B}_K(V_{j+1}) \\ \mathbf{C}_K(V_{j+1}) & 0 \end{bmatrix} \quad (2.19)$$

in which $\bar{V} \in [V_j, V_{j+1}]$ ($j < 14$) [25]. α_1 and α_2 can be any continuous functions of \bar{V} satisfying $\alpha_1 \geq 0$, $\alpha_2 \geq 0$, and $\alpha_1 + \alpha_2 = 1$. Here we set $\alpha_1 = \frac{V_{j+1} - \bar{V}}{V_{j+1} - V_j}$ and $\alpha_2 = \frac{\bar{V} - V_j}{V_{j+1} - V_j}$. When \bar{V} falls outside $[V_1, V_{15}]$, $\mathbf{K}_p(\bar{V})$ chooses the state-space data at either V_1 or V_{15} whichever is closer to \bar{V} .

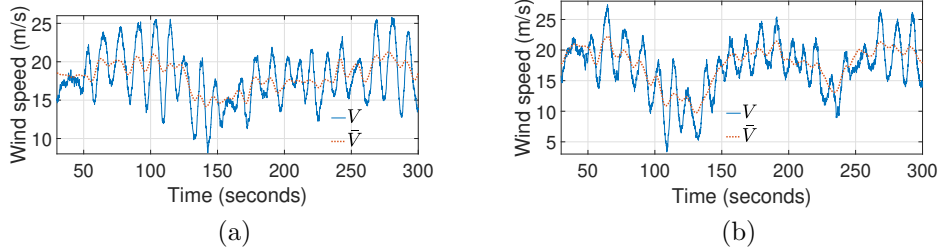


Figure 5: Real and LIDAR-previewed REWS's (V and \bar{V}) under the two turbulent wind profiles (with an average speed of 18 m/s) generated using the NTM (upper) and ETM (lower) respectively.

The AW compensator for the LPV blade pitch controller is designed in the same way as that in our paper [20]. However, the open-loop plant therein is affinely dependent on the wind speed, which is not the case here. So like what is detailed above for the calculation of the LPV pitch controller, the AW

Table 1: Comparison of the PI, PI AW, and LPV AW blade pitch controllers under a wind (see Figure 5a) and wave profile. The values in the brackets indicate the differences compared with the PI control case.

	PI	PI AW	LPV AW
Average power (kW)	4310.08	4306.58 (-0.08%)	4461.25 (3.51%)
Standard deviation of power (kW)	907.19	904.77 (-0.27%)	666.57 (-26.52%)
Standard deviation of pitch rate (deg)	10.80	10.80 (0%)	3.43 (-68.24%)
Fore-aft DEQL (kN·m)	73769.87	73562.77 (-0.28%)	58358.45 (-20.89%)
Standard deviation of barge pitch displacements (deg)	3.61	3.62 (0.28%)	3.04 (-15.79%)

compensator needs to satisfy multiple LMIs evaluated at the gridded points within the Region-3 wind speed range. Both the LPV pitch controller and its anti-windup system are scheduled by \bar{V} previewed by a LIDAR simulator whose development was detailed in our paper [20].

3. Simulation Study

Our LPV AW pitch controller is tested using the transformed barge HWT model and compared with the PI pitch controller designed by us in the paper [22] for the same barge HWT, through simulations in the MATLAB/Simulink environment. The back-calculation anti-windup method is selected for the PI controller with the back-calculation gain specified to be 0.5. For the simulations, we choose the ode4 solver (a fixed-step solver using the fourth-order Runge-Kutta formula for time integration) with the sampling frequency set to be 40 Hz.

The simulations employ two types of IEC full-field turbulent wind inputs with a same irregular wave input. The wind inputs are generated by Turb-

Table 2: Comparison of the PI, PI AW, and LPV AW blade pitch controllers under a wind (see Figure. 5b) and wave profile. The values in the brackets indicate the differences compared with the PI control case.

	PI	PI AW	LPV AW
Average power (kW)	3983.39	4056.24 (1.83%)	4501.30 (13.00%)
Standard deviation of power (kW)	1224.10	1215.28 (-0.72%)	617.46 (-49.56%)
Standard deviation of pitch rate (deg)	10.85	10.92 (0.65%)	5.23 (-51.80%)
Fore-aft DEQL (kN·m)	84367.64	81363.111 (-3.56%)	59419.991 (-29.57%)
Standard deviation of barge pitch displacements (deg)	4.33	4.14 (-4.39%)	2.98 (-31.18%)

231 Sim [26] using the IEC Kaimal spectral model. They use the NTM (Normal
232 Turbulence Model) with category A as the turbulence intensity and the Class
233 1 ETM (Extreme Turbulence Model), respectively. The longitudinal compo-
234 nents of both wind velocity inputs have a same mean value of 18 m/s at
235 the hub height. FAST HydroDyn [27] is employed to generate the waves
236 using the JONSWAP spectrum. The irregular waves are characterised by
237 the significant wave height (set to be 6 m) and peak period (set to be 10
238 seconds).

239 The real REWS V (from FAST AeroDyn) and its LIDAR-previewed value
240 \bar{V} are illustrated in Figure 5. It is clear that their low-frequency correlation
241 is good while low-frequency components affect a wind turbine most [28].

242 The comparisons of the PI, PI AW, and LPV AW blade pitch controllers
243 under the 2 different wind inputs are given in Tables 1 and 2, respectively.
244 These cases use a same torque controller synthesised in a similar way as in our
245 paper [20]. Here the damage to the blade bearings caused by pitch activities
246 is assessed by the standard deviation of collective pitch rates [29]. The time-
247 series of the tower base fore-aft bending moment is used to compute the fore-
248 aft damage equivalent load (DEQL) at the tower base by the NREL MLife

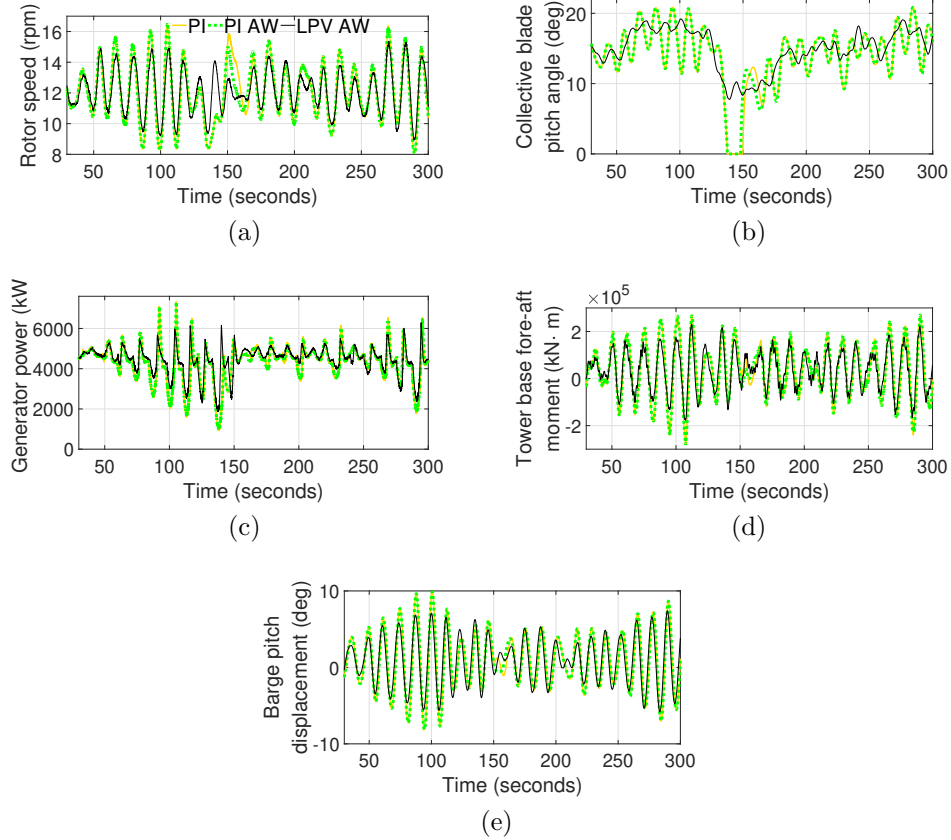


Figure 6: Responses under a wind (see Figure 5a) and wave profile. Figures 6a, 6b, 6c, 6d, and 6e show the rotor speed, collective blade pitch angle, generator power, tower base fore-aft moment, and barge pitch displacement, respectively.

code [30]. Tables 1 & 2 show that our LPV AW blade pitch controller attains much better overall performances than the PI and PI AW controllers in terms of much suppressed barge pitch motions, considerably reduced damage on the blade bearings & tower, less fluctuating rotor speed & generator power, and more power delivered. Figures 6 and 7 show the simulation results for the cases using the three types of pitch controllers, which verify the results in Tables 1 and 2 respectively. Additionally, Table 2 shows that significant rotor speed, generator power and tower fore-aft loading variations occur due to the pitch saturation during the transition at about 135 s (see Figure 5b) for the case using the PI (without AW) blade pitch controller, while the PI AW and

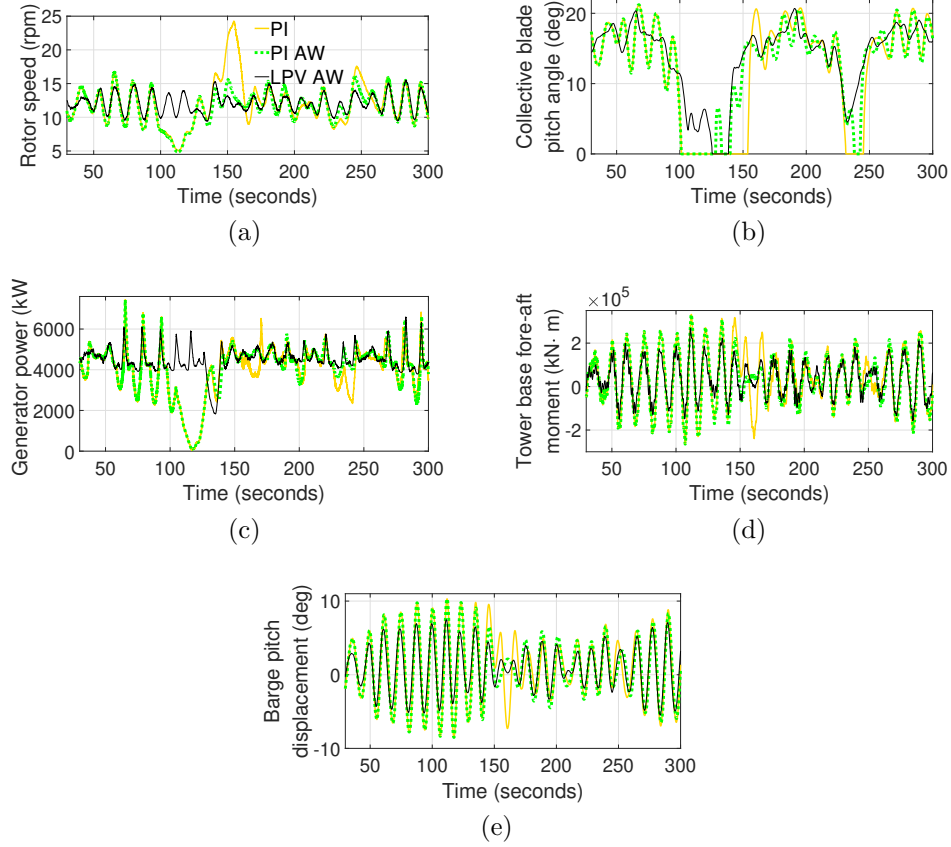


Figure 7: Responses under a wind (see Figure 5b) and wave profile. Figures 7a, 7b, 7c, 7d, and 7e show the rotor speed, collective blade pitch angle, generator power, tower base fore-aft moment, and barge pitch displacement, respectively.

259 LPV AW controllers achieve much smoother responses.

260 4. Discussion

261 The results indicate that the LPV AW collective blade pitch controller
 262 achieved appreciable reductions in power fluctuations, blade pitch actuator
 263 usage, fore-aft tower fatigue loads, and barge-pitch vibrations. We did not
 264 investigate how to control other dynamics like blade in-plane & out-of-plane
 265 motions and side-to-side turbine dynamics because we aim to specifically
 266 tackle fore-aft turbine vibrations (recall that the fore-aft direction suffers the

267 largest loading from winds and waves). Some unconsidered dynamics could
 268 deteriorate due to their coupling with blade pitch motions. We mention
 269 that our control strategy is quite flexible to be upgraded to deal with addi-
 270 tional dynamics. For example, to take into account side-to-side vibrations,
 271 the barge roll mode coupled with the first tower side-to-side bending mode,
 272 and generator torque dynamics can be added to the current control-oriented
 273 model. Then the procedure given in Section 2.2 can be followed to design
 274 the LPV AW controller based on the augmented control-oriented model with
 275 additional states, input (associated with generator torque in this example),
 276 and outputs (associated with tower side-to-side and barge roll motions in this
 277 example). By reasonably selecting weighting functions, power regulation and
 278 reduction of both fore-aft & side-to-side vibrations could be achieved through
 279 cooperative control of generator torque & blade pitch. Besides, individual
 280 blade pitch control can be a complement to the collective blade pitch con-
 281 trol to enable the reduction of asymmetric or periodic blade loads while the
 282 collective control only deals with symmetric dynamics [31, 32, 33].

283 Another approach to damp turbine vibrations is through applying pas-
 284 sive vibration damping devices whose design is generally independent of the
 285 design of other typical turbine controllers. A drawback of this type of meth-
 286 ods is that it needs extra components, e.g. a large mass, which is often not
 287 feasible except some existing components can be used. For the floating barge
 288 HWT considered here, its hydraulic reservoir can be shaped into a bidirec-
 289 tional tuned liquid column damper (BTLCD) and fixed onto the barge to
 290 damp pitch & roll motions of the barge without adding much extra costs
 291 [22]. Furthermore, the BTLCD can be connected to the tower base through
 292 springs and dampers, which allows it to move freely like a tuned mass damper
 293 (TMD). In this way, the advantages of the BTLCD and TMD are integrated
 294 to further suppress barge motions [14].

295 The proposed LPV AW controller has not been implemented on a real
 296 wind turbine. Before practical application, it is worthwhile to investigate how
 297 the selection of the resolution of grid points could affect control performances.
 298 We selected the grid points in a relatively conservative way. However, it is
 299 possible that good performance can still be achieved even with a smaller
 300 resolution.

301 5. Conclusions

302 We developed a LIDAR-based LPV AW pitch controller for a floating
303 barge hydrostatic wind turbine (HWT). It can simultaneously reduce the
304 barge pitch motions and regulate the power in Region 3, which would nor-
305 mally disturb each other if addressed separately. We tested its performances
306 using a transformed high-fidelity barge HWT simulation model taking into
307 account aerodynamics, hydrodynamics, servo-dynamics, and elastic dynam-
308 ics. The results showed much improved overall performances attained by our
309 controller in comparison with a gain-varied PI controller, in terms of barge
310 pitch suppression, load reductions of blade bearings & tower, rotor speed
311 regulation, and power quality.

312 6. Acknowledgement

313 This work was funded by the UK Engineering and Physical Sciences Re-
314 search Council under grant EP/S000747/1.

315 References

- 316 [1] A. Kuriqi, A. N. Pinheiro, A. Sordo-Ward, L. Garrote, Flow regime
317 aspects in determining environmental flows and maximising energy pro-
318 duction at run-of-river hydropower plants, *Applied Energy* 256 (2019)
319 113980.
- 320 [2] R. Godina, E. M. Rodrigues, E. Pouresmaeil, J. C. Matias, J. P. Catalão,
321 Model predictive control home energy management and optimization
322 strategy with demand response, *Applied Sciences* 8 (2018) 408.
- 323 [3] A. Razmjoo, M. Qolipour, R. Shirmohammadi, S. M. Heibati, I. Faraji,
324 Techno-economic evaluation of standalone hybrid solar-wind systems for
325 small residential districts in the central desert of iran, *Environmental*
326 *progress & sustainable energy* 36 (2017) 1194–1207.
- 327 [4] J. Lee, F. Zhao, Global Wind Report 2019, Technical Report, Global
328 Wind Energy Council, Brussels, Belgium, 2020.
- 329 [5] A. Pullen, M. G. Eneland, Global Wind 2006 Report, Technical Report,
330 Global Wind Energy Council, Brussels, Belgium, 2007.

- 331 [6] Prime minister’s office, The queen’s speech 2019, 2019.
- 332 [7] A. Nghiem, I. Pineda, Wind energy in Europe: Scenarios for 2030, Tech-
333 nical Report, WindEurope, Brussels, Belgium, 2017.
- 334 [8] IRENA, Future of wind: Deployment, investment, technology, grid in-
335 tegration and socio-economic aspects (A Global Energy Transformation
336 paper), Technical Report, International Renewable Energy Agency, Abu
337 Dhabi, United Arab Emirates, 2019.
- 338 [9] J.-C. Ossyra, Reliable, Lightweight Transmissions For Off-Shore, Utility
339 Scale Wind Turbines, Technical Report, Eaton Corporation, WI, USA,
340 2012.
- 341 [10] J. Carroll, A. McDonald, D. McMillan, Failure rate, repair time and
342 unscheduled O&M cost analysis of offshore wind turbines, Wind Energy
343 19 (2015) 1107–1119.
- 344 [11] S. Sheng, Report on Wind Turbine Subsystem Reliability—A Survey
345 of Various Databases, Technical Report, National Renewable Energy
346 Laboratory, CO, USA, 2013.
- 347 [12] L. Ran, P. A. Mawby, P. McKeever, S. Konaklieva, Condition monitor-
348 ing of power electronics for offshore wind, Engineering & Technology
349 Reference (2012) 1–10. DOI: 10.1049/etr.2014.0004.
- 350 [13] R. Dutta, Modeling and Analysis of short term energy storage for mid-
351 size hydrostatic wind turbine, Master’s thesis, University of Minnesota,
352 2012.
- 353 [14] X. Wei, X. Zhao, Vibration suppression of a floating hydrostatic wind
354 turbine model using bidirectional tuned liquid column mass damper,
355 Wind Energy 23 (2020) 1887–1904.
- 356 [15] J. M. Jonkman, Dynamics modeling and loads analysis of an offshore
357 floating wind turbine, Technical Report, National Renewable Energy
358 Laboratory, CO, USA, 2007.
- 359 [16] B. Skaare, B. Hörnsten, F. G. Nielsen, Modeling, simulation and control
360 of a wind turbine with a hydraulic transmission system, Wind Energy
361 16 (2013) 1259–1276.

- 362 [17] A. J. Laguna, Modeling and analysis of an offshore wind turbine with
 363 fluid power transmission for centralized electricity generation, *Journal*
 364 *of Computational and Nonlinear Dynamics* 10 (2015) 041002.
- 365 [18] B. Dolan, H. Aschemann, Control of a wind turbine with a hydrostatic
 366 transmission—an extended linearisation approach, in: 17th Interna-
 367 tional Conference on Methods and Models in Automation and Robotics
 368 (MMAR), Miedzyzdroje, Poland, 2012.
- 369 [19] J. Kersten, H. Aschemann, LMI approaches for a robust control of a
 370 wind turbine with a hydrostatic transmission, in: European Control
 371 Conference, Aalborg, Denmark, 2016.
- 372 [20] X. Tong, X. Zhao, Power generation control of a monopile hydrostatic
 373 wind turbine using an \mathcal{H}_∞ loop-shaping torque controller and an LPV
 374 pitch controller, *IEEE Transactions on control systems technology* 26
 375 (2018) 2165–2172.
- 376 [21] J. M. Jonkman, M. L. Buhl Jr, FAST user’s guide, Technical Report,
 377 National Renewable Energy Laboratory, CO, USA, 2005.
- 378 [22] X. Tong, X. Zhao, A. Karcianas, Passive vibration control of an offshore
 379 floating hydrostatic wind turbine model, *Wind Energy* 21 (2018) 697–
 380 714.
- 381 [23] D. Schipf, E. Simley, F. Lemmer, L. Y. Pao, P. W. Cheng, Collective
 382 pitch feedforward control of floating wind turbines using lidar, *Journal*
 383 *of Ocean and Wind Energy* 2 (2015) 223–230.
- 384 [24] P. Apkarian, R. J. Adams, Advanced gain-scheduling techniques for
 385 uncertain systems, *IEEE Transactions on control systems technology* 6
 386 (1998) 21–32.
- 387 [25] P. Apkarian, P. Gahinet, G. Becker, Self-scheduled \mathcal{H}_∞ control of linear
 388 parameter-varying systems: A design example, *Automatica* 31 (1995)
 389 1251–1261.
- 390 [26] B. J. Jonkman, TurbSim user’s guide: Version 1.50, Technical Report,
 391 National Renewable Energy Laboratory, CO, USA, 2009.

- 392 [27] J. Jonkman, A. Robertson, G. Hayman, HydroDyn user's Guide and
393 Theory Manual, Technical Report, National Renewable Energy Labora-
394 tory, CO, USA, 2014.
- 395 [28] F. Dunne, L. Y. Pao, D. Schlipf, A. K. Scholbrock, Importance of
396 lidar measurement timing accuracy for wind turbine control, in: 2014
397 American Control Conference, OR, USA, 2014.
- 398 [29] K. Z. Østergaard, J. Stoustrup, P. Brath, Linear parameter varying
399 control of wind turbines covering both partial load and full load condi-
400 tions, *International Journal of Robust and Nonlinear Control* 19 (2009)
401 92–116.
- 402 [30] G. J. Hayman, MLife theory manual for version 1.00, Technical Report,
403 National Renewable Energy Laboratory, CO, USA, 2012.
- 404 [31] H. Namik, K. Stol, Individual blade pitch control of floating offshore
405 wind turbines, *Wind Energy* 13 (2010) 74–85.
- 406 [32] S. Sarkar, B. Fitzgerald, B. Basu, Individual blade pitch control of
407 floating offshore wind turbines for load mitigation and power regulation,
408 *IEEE Transactions on Control Systems Technology* (2020) 1–11. DOI:
409 10.1109/TCST.2020.2975148.
- 410 [33] Y. Yuan, X. Chen, J. Tang, Multivariable robust blade pitch control
411 design to reject periodic loads on wind turbines, *Renewable Energy* 146
412 (2020) 329–341.